THE JOURNAL OF PHYSICAL CHEMISTRY C

pubs.acs.org/JPCC Article

Broadband Colossal Dielectric Constant in the Superionic Halide $RbAg_4I_5$: Role of Intercluster Ag^+ Diffusion

Paribesh Acharyya, Tanmoy Ghosh, Shidaling Matteppanavar, Raju K. Biswas, Premakumar Yanda, Srinivasa R. Varanasi, Dirtha Sanyal, A. Sundaresan, Swapan K. Pati, and Kanishka Biswas*

Cite This: J. Phys. Chem. C 2020, 124, 9802–9809 Read Online

ACCESS | Metrics & More | Article Recommendations | Supporting Information

ABSTRACT: Materials with ultrahigh dielectric constants and a low value of dielectric loss are important for energy storage and electronic devices. Traditionally, high dielectric constant is found in ferroelectric complex oxides, but they exhibit high dielectric loss as well. Herein, a broadband colossal dielectric constant in a superionic halide, $RbAg_4I_5$, with a low dielectric loss is presented. The real part of the dielectric constant, ε', increases by 10^2 orders of magnitude as $RbAg_4I_5$ goes through a superionic transition at 121 K. At room temperature, $\varepsilon' > 10^6$ in the frequency range 10^{-1} to 10^4 Hz with a low dielectric loss, which ranges between 2.03 and 0.53. The maximum of ε' reaches a colossal value of 6.4×10^8 at 0.1 Hz at 300 K. The molecular dynamics simulation reveals the presence of Ag^+ clusters with a broad size distribution. The intercluster diffusion of Ag^+ causes significant instantaneous charge separation and a consequent large fluctuation in the dipole moments. The fluctuating dipoles, in turn, result in the colossal dielectric constant in $RbAg_4I_5$.

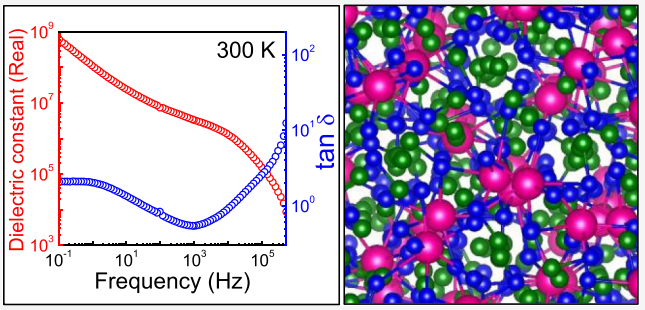

INTRODUCTION

The development of materials with a colossal dielectric constant (CDC) is an integral part of advancing the modern electronics, sensors, and energy-storage devices.[1−6] Traditionally, high dielectric constant is associated with ferroelectric oxides across their paraelectric to ferroelectric transition, where $\varepsilon' \approx 10^3$ to 10^4 can be easily achieved.[7−12] Recently, few complex oxides have also emerged as nonferroelectric high dielectric constant materials where high ε' arises either from polarization relaxation and polar fluctuations in nanosize domains or from Maxwell−Wagner polarization in the grain boundaries.[13−18] One of the most notable examples is the double-perovskite $CaCu_3Ti_4O_{12}$ (CCTO) in which CDC with $\varepsilon' \approx 10^4$ to 10^5 has been achieved over a broad temperature and frequency range, although the exact origin of the CDC in CCTO is still under debate.[19−22] However, most of these oxides have a high dielectric loss, tan δ, as well. Low-dimensional systems with a charge density wave also show a high dielectric constant; however, the associated tan δ is high.[23,24] Recently, another intriguing category of materials, called superionic conductors, are emerging as high dielectric constant materials with a low tan δ.[25−27] The perovskite oxide superionic conductor $Rb_2Ti_2O_5$ exhibited a dielectric constant $\varepsilon' \approx 10^9$ at 0.01 Hz at 300 K.[25]

Superionic conductors are solid materials with a high ionic conductivity ($\sigma > 10^{-3}$ S/cm; in ordinary solid $\sigma \approx 10^{-8}$ S/cm).[28,29] For example, the room-temperature ionic conductivities of the superionic compounds $Rb_2Ti_2O_5$ and $RbAg_4I_5$ are $\sim 10^{-3}$ and ~ 0.2 S/cm, respectively.[25,30] Such a high ionic conductivity is, in general, thought to be detrimental to achieving CDC in a material. One of the requirements for observing CDC in superionic conductors is that the material must have very low electronic conductivity. For example, $Rb_2Ti_2O_5$ has room-temperature electronic conductivity $\sim 10^{-8}$ S/cm.[25] The room-temperature electronic conductivity of the present $RbAg_4I_5$ is $\sim 10^{-9}$ S/cm, which satisfies the required condition.[31,32] Superionicity in a material is induced when highly disordered cation sites are present along with polar states.[33] The polar states are created by the charge transfer due to ion migrations to the interstices. Consequently, these ionic migrations may create dipoles in the lattice, which is probably important to have a high dielectric constant. $RbAg_4I_5$ exhibits a complex crystal structure[34−36] with a large number of Ag^+ present in the lattice, which migrate to the interstitial positions in its superionic phase, and therefore, $RbAg_4I_5$ is expected to show CDC.

Herein, we have demonstrated a broadband CDC with a low dielectric loss in superionic $RbAg_4I_5$, which is synthesized by a

Received: March 10, 2020
Revised: April 11, 2020
Published: April 14, 2020

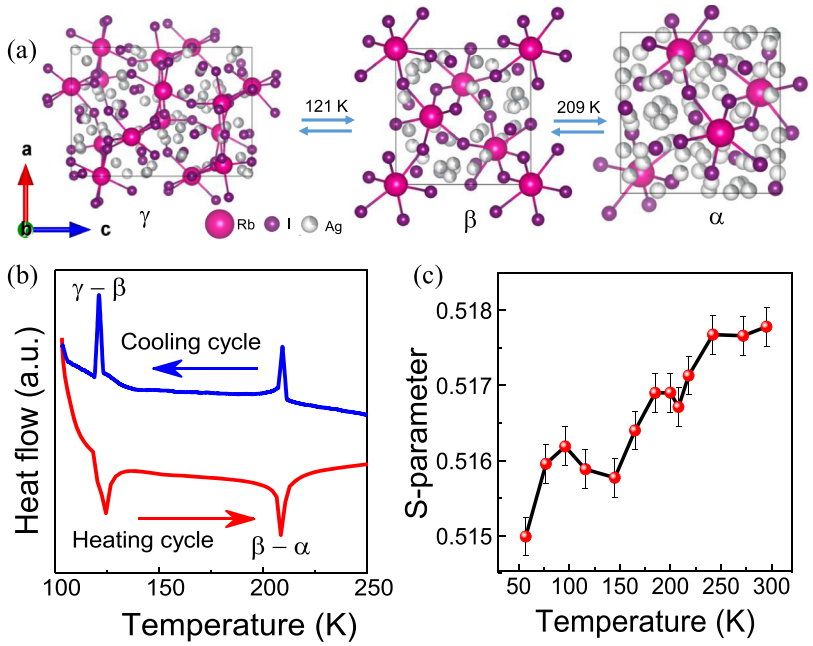

Figure 1. (a) Cubic α-phase, rhombohedral β-phase, and trigonal γ-phase of $RbAg_4I_5$. (b) DSC signal showing the structural phase transitions in $RbAg_4I_5$. (c) Temperature dependence of the S-parameter obtained from PAL spectroscopy.

facile, solvent-free mechanochemical synthesis at room temperature. The presence of two structural phase transitions with decreasing temperature, α (cubic, space group $P4_332$; Figure 1a) $\rightarrow \beta$ (rhombohedral, space group R32; Figure 1a) at 209 K and $\beta \rightarrow \gamma$ (trigonal, space group $P321$; Figure 1a) at 121 K, has been confirmed via temperature-dependent powder X-ray diffraction (PXRD) and differential scanning calorimetry (DSC). The temperature-dependent positron annihilation lifetime (PAL) spectroscopy and coincidence Doppler broadening (CDB) spectra evidence the presence of charged vacancies associated with the diffusion of Ag^+. We have shown that ε' increases by 10^2 orders of magnitude as $RbAg_4I_5$ goes through the $\gamma \rightarrow \beta$ superionic phase transition from the low-temperature side, and ε' reaches a giant value $\sim 6.4 \times 10^8$ at 0.1 Hz in the room-temperature superionic α phase. The molecular dynamics (MD) simulation shows charge density fluctuation within Ag^+ clusters because of intercluster Ag^+ diffusion. This causes fluctuation in the instantaneous dipole moments associated with Ag^+ clusters and results in the experimentally observed CDC in the room-temperature superionic phase of $RbAg_4I_5$.

METHODS

Experimental Section. *Starting Materials.* Rubidium (I) iodide (RbI, 99.5%) and silver (I) iodide (AgI, 99.999%) were purchased from Sigma Aldrich and used without further purification during synthesis.

Methods of Synthesis. For the $RbAg_4I_5$ synthesis, 939 mg of AgI (4 mmol) and 212.4 mg (1 mmol) of RbI were taken as precursors in a mortar and pestle. The precursors were mechanically ground and mixed thoroughly in the mortar and pestle for about 2 h under inert condition (N_2-filled glove bag).

The following scheme is implemented to synthesize high-quality polycrystals of $RbAg_4I_5$

$$RbI + 4AgI \xrightarrow{\text{mechanochemistry}} RbAg_4I_5$$

The polycrystalline pellets of $RbAg_4I_5$ (Figure S1, Supporting Information) were obtained thorough spark plasma sintering (SPS) using a SPS211-LX, Dr. Sinter Lab SPS machine. SPS was carried out at 120 °C under an applied pressure of 50 MPa for 20 min. The SPS-processed sample was polished and used for PAL spectroscopy and dielectric measurements.

PXRD. A Rigaku Smart Lab X-ray diffractometer equipped with a Cu Kα (wavelength = 1.54059 Å) X-ray source was used to acquire the temperature-dependent PXRD patterns of as-synthesized $RbAg_4I_5$ at 80, 180, and 300 K.

DSC. Finely ground powder samples were used for DSC measurements, in which the data were collected in a wide temperature range from 100 to 300 K by using a METTLER TOLEDO differential scanning calorimeter (DSC 822 e) at a fixed heating/cooling rate of 1 K/min.

PAL and CDB Spectroscopies. The PAL spectra was measured by the standard fast γ–γ coincidence technique by utilizing two BaF_2 ultrafast scintillators coupled with a XP2020Q photomultiplier tube. An approximately 10 μCi ^{22}NaCl positron-emitting source sealed in a thin mylar foil was sandwiched between two identical pellets of the $RbAg_4I_5$ sample. The specific experimental setup can be found in an earlier report.[37] The acquired life-time spectrum has been deconvoluted to reveal the lifetime values by the computer program, PATFIT-88,[38] after considering proper source correction.

An HPGe detector was exploited for the detection of Doppler broadening, originating from the positron annihilation γ-ray of 511 keV. An energy resolution of 1.15 from ^{85}Sr at 514 keV possesses an efficiency equivalent to 12% (model number PGC 1216sp of DSG, Germany). The details of the experimental setup are described in an earlier report.[39]

The CDB spectroscopic method was employed to recognize either the chemical features of the defect or the potential rationale for the enhancement in the *S*-parameter. The CDB experiments were carried out by using two analogous HPGe detectors of 12% efficiency with the model number PGC 1216sp

https://dx.doi.org/10.1021/acs.jpcc.0c02118
J. Phys. Chem. C 2020, 124, 9802−9809

of DSG, Germany. The peak to background ratio for the present CDB setup with ± ΔE selection is better than 105:1. Details of the experimental setup are depicted in an earlier report.[39]

S-Parameter can be designated as the ratio of the counts within the energy range of $|511\ \text{keV} - E| \leq 0.85$ keV to the total counts within the energy range of $|511\ \text{keV} - E| \leq 4.25$ keV under the photopeak of 511 keV.

Dielectric Measurements. The temperature- and frequency-dependent dielectric properties were determined in a physical property measurement system (Quantum Design, USA) using an Agilent E4980A LCR meter within the frequency range of 20 Hz to 200 kHz. The room-temperature dielectric properties were obtained using a Solartron 1260A impedance analyzer from the frequency of 0.1 Hz to 500 kHz. These measurements were conducted in the parallel plate geometry, in which Pelco high-performance silver paste from TED PELLA was coated on either side of the disk-shaped pellet sample.

I−V Measurement. The room-temperature $I-V$ curve of $RbAg_4I_5$ (Figure S2, Supporting Information) was measured using a rectangular bar of dimensions ∼2 × 2 × 8 mm, which was obtained after polishing an SPS processed pellet specimen in a ULVAC-RIKO ZEM-3 instrument.

Theoretical Section. *MD Simulation.* The interactions between Ag^+-Ag^+, Ag^+-I^-, Ag^+-Rb^+, and I^-I^- have been modeled using the Vasishta−Rahman potential.[40]

$$\phi_{ab}^{VR} = \frac{Z_a Z_b e^2}{r_{ab}} + \frac{A(\sigma_a + \sigma_b)^{n_{ab}}}{r_{ab}^{n_{ab}}} - \frac{w_{ab}}{r_{ab}^6} - \frac{(\alpha_a Z_b^2 + \alpha_b Z_a^2)/2}{r_{ab}^4} \quad (1)$$

where r_a, r_b, and r_{ab} are the positions of the ions a and b and the distance between them, respectively. A is the repulsive strength; σ_a and σ_b are the ionic radii; α_a and α_b are the electronic polarizabilities; and Z_a and Z_b are the fractional charges on the ions a and b, respectively. Electronic polarizabilities of Ag^+ and Rb^+ have been taken to be zero since they are relatively smaller in size than I^-. n_{ab} is the degree of hardness of the repulsive interaction between the ions a and b.

The interaction between Rb^+-Rb^+ and Rb^+-I^- has been modeled with the Born−Mayer potential[40]

$$\phi_{ab}^{BM} = \frac{Z_a Z_b e^2}{r_{ab}} + B_{ab} e^{-\gamma r_{ab}} - \frac{C_{ab}}{r_{ab}^6} - \frac{D_{ab}}{r_{ab}^8} \quad (2)$$

where the first and second terms emerged from the Coulomb interactions between two point charges and the overlap between the outer shell electrons of corresponding ions, respectively. Furthermore, the third and fourth terms appeared due to van der Waals interactions. The parameters related to the above-mentioned interaction potentials have been extracted from the work of Tahara and Fukami.[40]

We have taken the crystal structure of α-$RbAg_4I_5$ as our starting configuration, and the unit cell has been replicated three times in each direction to form a larger cubic simulation box. The simulation box contains 2560 atoms in total. MD simulations were performed in the NPT ensemble under ambient conditions for about 3 ns to obtain an equilibrated volume of the simulation cell. A time step of 1 fs was used in the velocity form of Verlet integrator. We implemented the simulation in the microcanonical (NVE) ensemble for about 3 ns to equilibrate the system at 298 K. After achieving the equilibration, further MD simulation was executed for 10 ns during which the trajectories were stored every 10 fs. In order to calculate the electrostatic interactions, Ewald summation technique was utilized. All interactions were truncated using a cutoff distance of 1.8 nm. Periodic boundary conditions were employed in all directions in order to ensure that there are no surface effects at the boundaries.

Connectivity Analysis and Cluster Size Estimation. Further to study the ordering arrangement of Ag^+ ions, connectivity analysis was carried out on the equilibrated atomic configurations procured from the MD simulations. In the connectivity analysis, we considered that the neighboring atoms formed clusters of various sizes within the first correlation length, corresponding to the first peak position in $g_{ab}(r)$. The dimensions of such cluster sizes are estimated by the number of ions present in the cluster within the first peak in the radial distribution function. The size distributions of these clusters were estimated by considering an average of 25 atomic configurations, each of which was obtained after consecutive 2000 MD time steps.

Diffusion Coefficient Calculation. To further validate our results, we investigated the dynamical properties of Ag^+, which correspond to the time correlation functions. These functions are further associated with the values obtained on different time scales (t) by assuming that the system is in equilibrium as well as independent of the choice of origin. The time evolution of ionic configurations in the simulation cell was implemented to calculate the physical quantity equivalent of the ionic transport properties, which is as follows. The following equation of mean square displacement (MSD) can be expressed as

$$\langle r_a^2(t) \rangle = \frac{1}{N_a} \sum_{i_a=1}^{N_a} \langle |r_{i_a}(t) - r_{i_a}(0)|^2 \rangle \quad (3)$$

where the total number of a-type ions can be denoted by the N_a term. MSD curves plotted as a function of MD time steps for Rb^+, Ag^+, and I^- are shown in Figure S3, Supporting Information. We notice that the diffusive behavior of Ag^+ is more prominent compared to all other types of ions. Once MSD is calculated, the diffusion coefficient (D) can be estimated from the linear regime in the MSD curve of Ag^+ ions at $t \to \infty$, that is,

$$D = \lim_{t \to \infty} \frac{r_a^2(t)}{6t} \quad (4)$$

Dipole Moment Calculation. The dipole moment (M) of component x at time step t of a MD simulation trajectory is calculated by the expression[41]

$$M_{x,t} = \sum_{k=1}^{N} q_k r_{k,t} \quad (5)$$

where r_k, N, and q_k are the position coordinate of atom k, the total number of atoms in the simulation box, and the charges, respectively. It is important to mention that the calculation of the dipole moment relied on the choice of the basis of the coordinate system. For our model, the dipole moment was evaluated in respect of the center of mass of the system. The static dielectric constant of a material follows the expression:[42]

$$\varepsilon = \frac{\langle M^2 \rangle - \langle M \rangle^2}{3V\varepsilon_0 k_B T} + 1 \quad (6)$$

https://dx.doi.org/10.1021/acs.jpcc.0c02118
J. Phys. Chem. C 2020, 124, 9802−9809

where V, k_B, ε_0, and T are the volume of the supercell, the Boltzmann constant, the permittivity of free space, and the absolute temperature, respectively.

RESULTS AND DISCUSSION

$RbAg_4I_5$ is a well-known prototypical superionic conductor with a very high ionic conductivity of ~0.2 S/cm at room temperature.[30] The room-temperature superionic phase (α-phase) has a complex cubic crystal structure with four $RbAg_4I_5$ units in the unit cell.[34−36] Three types of crystallographically nonequivalent sites are present for Ag^+: one eight-fold (Ag-c sites) and two 24-fold sets (Ag−I and Ag-II sites). The superionicity in $RbAg_4I_5$ arises from the fast diffusion of Ag^+ (diffusion coefficient ~10^{-6} cm^2 s^{-1}) in a β-Mn-type rigid iodide sublattice.[34−36,43,44] The iodide substructure contains 56 iodide tetrahedra in which 16 Ag^+ are randomly distributed in the interstitial positions. The tetrahedral framework is arranged in such a fashion that they create a network of passageways for the diffusion of Ag^+. The room-temperature cubic α-phase of $RbAg_4I_5$ is preceded by two structural phase transitions with decreasing temperature: a weak first-order $\alpha \rightarrow \beta$ phase transition at 209 K and a first-order $\beta \rightarrow \gamma$ phase transition at 121 K.[35,45−48] Remarkably, the iodide substructure remains almost intact, suffering only minor distortions to accommodate the partial ordering of Ag^+ at specific sites, across all these phase transitions.[35] The partial ordering of Ag^+ in the β phase restricts the movement of Ag^+ along the crystallographic c-axis, which decreases the ionic conductivity. Interestingly, Ag^+ remains partially disordered in the lowest temperature γ phase; however, the Ag^+ ionic diffusion occurs only within isolated clusters.[36]

Here, we have carried out a facile solvent-free mechanochemical synthesis of $RbAg_4I_5$ at room temperature (see details in experimental section). The presence of two sharp peaks in the DSC signal (Figure 1b) confirms the presence of two structural phase transitions at 209 and 121 K in the mechanochemically synthesized $RbAg_4I_5$. The temperature-dependent PXRD patterns at 300, 180, and 80 K are shown in Figure S4, Supporting Information. The Rietveld refinements of the temperature-dependent PXRD patterns confirm the room-temperature cubic (space group $P4_332$), mid-temperature rhombohedral (space group R32), and low-temperature trigonal (space group $P321$) structures corresponding to α, β, and γ phases, respectively. The two superionic α and β phases are differentiated only by a small distortion in the iodide sublattice. The obtained crystal structure parameters (Tables S1−S4, Supporting Information) for all three phases agree well with the previous reports.

The diffusion of Ag^+ creates charged vacancies in the system, which have been experimentally probed using PAL and CDB spectroscopies. The fitting of PAL spectra at 300 K (Figure S5a, Supporting Information) yields a short lifetime of 180 ± 2 ps of 20 ± 1% intensity and a longer component of 341 ± 5 ps with 80 ± 1% intensity. The positron trapped in a cation defect elapses for a longer time.[49] Therefore, the short lifetime component (180 ± 2 ps) has been assigned to the free annihilation of positrons, whereas the longer lifetime component (341 ± 5 ps) has been assigned to the positron annihilation at the vacancy sites.[49] The high intensity of the PAL component at the vacancy sites indicates the strong ionic character of the material as these charged vacancies are created because of the diffusion of Ag^+. The ionic conductivity of $RbAg_4I_5$ increases with increasing temperature because of increased diffusion of Ag^+.[43,44] As a result, charged vacancies also increase, and this is reflected in the gradual increase of the Doppler broadening S-parameter with increasing temperature (Figure 1c). Two anomalies corresponding to the $\gamma \rightarrow \beta$ and $\beta \rightarrow \alpha$ phase transitions with increasing temperature are also evident in the temperature variation of the S-parameter. The area-normalized ratio curve of the CDB spectra at 300 K with respect to the 50 K CDB spectra (Figure S5b, Supporting Information) shows a broad dip at the momentum value ~19×10^{-3} m °c. The corresponding energy value is 92 eV which is very close to the binding energy of the 4 s electron of Ag. This indicates that the positrons are less annihilating with the core electrons of Ag^+ at 300 K.

The experimentally measured temperature variations of the dielectric constant (ε') and dielectric loss (tan δ) at different frequencies ranging between 1 and 200 kHz are shown in Figures 2 and S6, Supporting Information. The presence of two

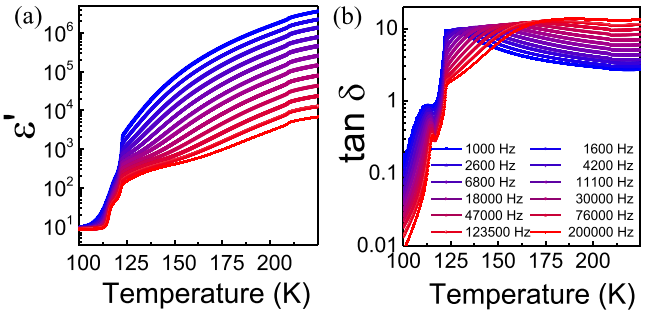

Figure 2. Temperature and frequency dependences of the (a) dielectric constant (ε') and (b) dielectric loss (tan δ) for $RbAg_4I_5$.

phase transitions, $\gamma \rightarrow \beta$ and $\beta \rightarrow \alpha$, with increasing temperature is evident from the temperature variations of ε' and tan δ. From the low-temperature side, ε' steeply increased by 10^1 to 10^2 orders of magnitude at the first-order superionic $\gamma \rightarrow \beta$ phase transition. For example, ε' at 1 kHz increases from 16.5 at 110 K to 3096 at 125 K. Correspondingly, tan δ exhibits a peak, which shifts to higher temperature with increasing frequency. ε' continues to increase gradually after the superionic $\gamma \rightarrow \beta$ phase transition with increasing temperature, except for a weak anomaly across the $\beta \rightarrow \alpha$ phase transition at 209 K. $RbAg_4I_5$ emerges to the superionic phase at the first structural transition ($\gamma \rightarrow \beta$ at ~121 K); therefore, the dielectric constant changes drastically across this transition. However, $RbAg_4I_5$ is already in the superionic regime when the second phase transition ($\beta \rightarrow \alpha$) occurs at ~209 K, and as a result, the change in dielectric response is not as dramatic as the one observed across the first structural transition ($\gamma \rightarrow \beta$) at ~121 K.

The experimentally obtained frequency dependence of the dielectric constant (ε') at 150 and 300 K corresponding to the superionic β and α phases, respectively, is shown in Figure 3a. At 300 K, ε' has a broadband colossal value >10^6 in the frequency range 10^{-1} to 10^4 Hz, with the maximum value reaching ~6.4×10^8 at 0.1 Hz. The corresponding dielectric loss (tan δ) in the frequency range 10^{-1} to 10^4 varies between 2.03 and 0.53, which is low (Figure 3b). A comparison of the room-temperature dielectric properties of $RbAg_4I_5$ with other high dielectric constant materials is listed in Table S5, Supporting Information. Ag^+ diffusion dominates the transport behavior of $RbAg_4I_5$ at 300 K. For such diffusion-dominated behavior, log|Z| (|Z| is the impedance magnitude) varies linearly with log f in the low-frequency region and has a slope −1/2 or −1/4.[50] This linear relationship between log|Z| and log f is evident in the low-frequency region at room temperature (Figure 3c). The

https://dx.doi.org/10.1021/acs.jpcc.0c02118
J. Phys. Chem. C 2020, 124, 9802−9809

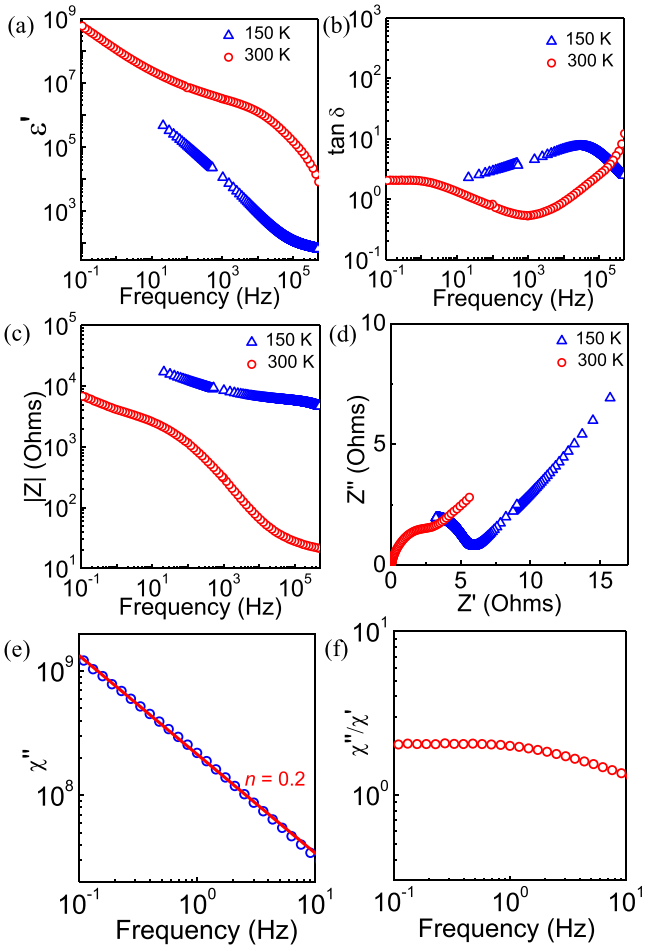

Figure 3. Frequency dependences of (a) the dielectric constant (ε'), (b) the dielectric loss (tan δ), (c) |Z|, and (d) Nyquist plots at 150 and 300 K. Room-temperature (e) $\chi''(\omega)$ and (f) $\chi''(\omega)/\chi'(\omega)$ exhibiting the universal dielectric response according to Jonscher's theory.

obtained slope is −0.234(2) in the frequency region 1−0.1 Hz. Furthermore, the Nyquist plot (Figure 3d) also shows a linear relationship between the real and imaginary parts of impedance, Z' and Z'', respectively, in the low-frequency region, indicating the diffusion-dominated behavior.

The observed dielectric properties of $RbAg_4I_5$ can also be reconciled with the universal dielectric response (UDR), as put forward by Jonscher.[51,52] According to the Jonscher's theory, the dielectric response of most materials follows a universal pattern, which in the frequency domain can be expressed as follows: (i) the frequency dependence of the imaginary part of complex susceptibility (χ) follows a sublinear power law, that is, $\chi''(\omega) \propto \omega^{n-1}$ with $0 < n < 1$ and (ii) the ratio $\chi''(\omega)/\chi'(\omega)$ is constant and independent of the frequency. In the case of ionic conductors, n has low values so that the exponent $(n - 1)$ is close to unity, which is often called as low-frequency dispersion (LFD). The frequency dependences of room-temperature $\chi''(\omega)$ and $\chi''(\omega)/\chi'(\omega)$ are shown in Figure 3e,f, respectively, which evidence that LFD of $RbAg_4I_5$ is in accordance with UDR with $n \approx 0.2$.

MD simulation was carried out in order to understand the origin of the experimentally observed broadband CDC behavior in the superionic $RbAg_4I_5$. The calculated partial radial pair distribution function $g_{ab}(r)$, which has been defined as $g_{ab}(r) = \frac{N_{ab}(r)}{4\pi r^2 \Delta r \rho_b}$ where $N_{ab}(r)$ is the number of b-type ions at a distance between r and $r + \Delta r$ from the central a-type ion and ρ_b is the mean number density of the b-type ions, from the equilibrated atomic configuration in the MD simulation cell at 298 K is shown in Figures 4a and S7a, Supporting Information. The partial radial distribution functions calculated from our model match reasonably well with those from other previous studies.[40,42] The first sharp peak in $g_{ab}(r)$ for the I^-−I^- pair at ∼4.28 Å and a deep minimum at ∼5.76 Å (Figure 4a) correspond to the first coordination between the I^-−I^- pair and indicates the structural ordering of I^-. Further, the presence of well-defined second and third peaks at ∼7.30 and ∼8.60 Å,

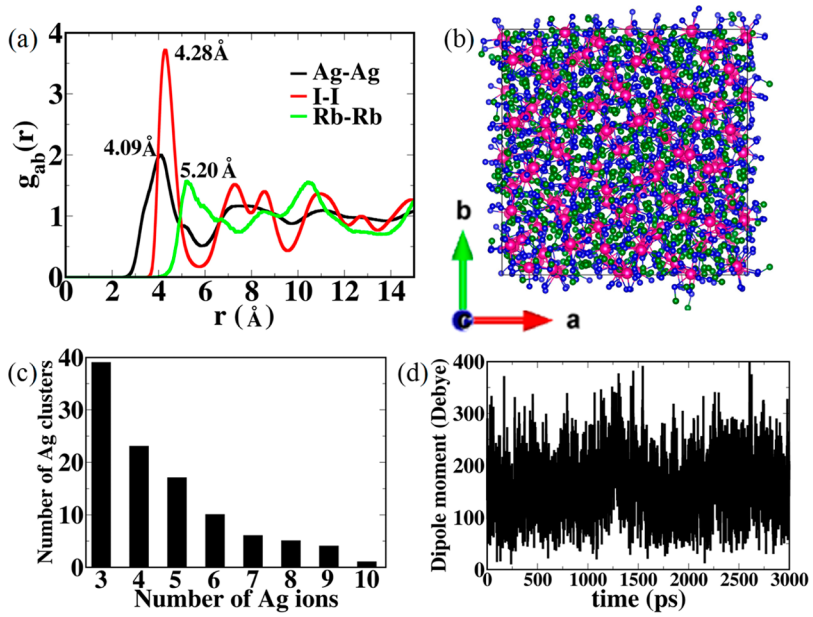

Figure 4. (a) Partial radial pair distribution function $g_{ab}(r)$ vs radial distance r between Ag^+−Ag^+, Rb^+−Rb^+, and I^-−I^- and (b) snapshot of the $RbAg_4I_5$ supercell obtained from MD simulation at 298 K; Ag, green; Rb, magenta; and I, blue. (c) Histogram showing the distribution of the Ag cluster. (d) Fluctuation in dipole moments at 298 K.

https://dx.doi.org/10.1021/acs.jpcc.0c02118
J. Phys. Chem. C 2020, 124, 9802−9809

respectively, in $g_{ab}(r)$ indicates the long-range ordering of I^-. The presence of the first sharp peak in $g_{ab}(r)$ corresponding to the first neighbor coordination for the Ag^+-I^- pair at ~2.62 Å (Figure S7a, Supporting Information) further indicates the ordered arrangement of I^- around Ag^+ throughout the solid. The first peak in $g_{ab}(r)$ for the Rb^+-I^- pair at ~3.30 Å (Figure S7a, Supporting Information) is also sharp, but the magnitude is lower than that of the Ag^+-I^- pair, which suggests that a greater number of Ag^+ are present in the surrounding of I^- than Rb^+. This particular arrangement formed by I^- enforces Ag^+ to come close to each other and make a collection of Ag^+ as a cluster. A similar signature is observed in $g_{ab}(r)$ for the Ag^+-Ag^+ pair (Figure 4a). Instead of complete randomness, $g_{ab}(r)$ for the Ag^+-Ag^+ pair shows a broad peak at ~4.10 Å corresponding to the nearest neighbor coordination; however, the long-range coordination peaks, such as for the second and third coordinations, are not well defined, which indicate clustering of Ag^+. Ag^+ accumulation within the network of channels created by I^- and the formation of Ag^+ clusters are evident from the snapshot of the $RbAg_4I_5$ supercell obtained from MD simulation (Figures 4b and S7b, Supporting Information). Rb^+, because of its large size, facilitates smooth conduction pathways for Ag^+ to hop from one cluster to another, which consequently results in the high diffusion coefficient. The calculated diffusion coefficient 0.383×10^{-5} cm^2/s (see Methods for the diffusion coefficient calculation) agrees well with the experimental reports.[43] This intercluster ionic diffusion leads to a broad size distribution of the clusters (Figure 4c) and large charge separations, which, in turn, lead to large fluctuations in the instantaneous dipole moments in the range between 25 and 300 Debye (see Methods for dipole moment calculation) (Figure 4d). Consequently, these large fluctuating dipole moments result in the high dielectric constant as observed in the experiment.

CONCLUSIONS

In conclusion, we have demonstrated an extremely high room-temperature ε' in the superionic halide $RbAg_4I_5$, which reaches a maximum value of $\sim 6.4 \times 10^8$ at 0.1 Hz. This colossal ε' persists over a wide frequency range along with a low dielectric loss. The frequency dependence of impedance indicates that ionic diffusion has the dominating contribution, which results in such a giant ε'. MD simulation further established that this colossal ε' arises because of intercluster Ag^+ diffusion, which causes a large charge separation and an associated fluctuation in the instantaneous dipole moments. The observed broadband colossal ε' in this nonoxide superionic solid opens up new opportunities in dielectric investigations and structure–property relationship in new halides.[53]

ASSOCIATED CONTENT

Supporting Information

The Supporting Information is available free of charge at https://pubs.acs.org/doi/10.1021/acs.jpcc.0c02118.

Refinement of X-ray diffraction, additional PAL and dielectric data, and additional MD results (PDF)

AUTHOR INFORMATION

Corresponding Author

Kanishka Biswas − *New Chemistry Unit and School of Advanced Materials and International Centre of Materials Science, Jawaharlal Nehru Centre for Advanced Scientific Research (JNCASR), Bangalore 560064, India;* orcid.org/0000-0001-9119-2455; Email: kanishka@jncasr.ac.in

Authors

Paribesh Acharyya − *New Chemistry Unit, Jawaharlal Nehru Centre for Advanced Scientific Research (JNCASR), Bangalore 560064, India*

Tanmoy Ghosh − *New Chemistry Unit, Jawaharlal Nehru Centre for Advanced Scientific Research (JNCASR), Bangalore 560064, India*

Shidaling Matteppanavar − *New Chemistry Unit, Jawaharlal Nehru Centre for Advanced Scientific Research (JNCASR), Bangalore 560064, India*

Raju K. Biswas − *Theoretical Sciences Unit, Jawaharlal Nehru Centre for Advanced Scientific Research (JNCASR), Bangalore 560064, India*

Premakumar Yanda − *Chemistry and Physics of Materials Unit, Jawaharlal Nehru Centre for Advanced Scientific Research (JNCASR), Bangalore 560064, India*

Srinivasa R. Varanasi − *Theoretical Sciences Unit, Jawaharlal Nehru Centre for Advanced Scientific Research (JNCASR), Bangalore 560064, India*

Dirtha Sanyal − *Variable Energy Cyclotron Centre, Kolkata 700064, India;* orcid.org/0000-0003-2490-3610

A. Sundaresan − *Chemistry and Physics of Materials Unit and School of Advanced Materials and International Centre of Materials Science, Jawaharlal Nehru Centre for Advanced Scientific Research (JNCASR), Bangalore 560064, India;* orcid.org/0000-0002-1613-3030

Swapan K. Pati − *Theoretical Sciences Unit and School of Advanced Materials and International Centre of Materials Science, Jawaharlal Nehru Centre for Advanced Scientific Research (JNCASR), Bangalore 560064, India;* orcid.org/0000-0002-5124-7455

Complete contact information is available at: https://pubs.acs.org/10.1021/acs.jpcc.0c02118

Notes

The authors declare no competing financial interest.

ACKNOWLEDGMENTS

This work was supported by the DST (DST/TMD/MES/2k17/24). P.A. acknowledges the UGC and Diptikanta Swain, IISc for PXRD measurements. R.K.B. acknowledges the UGC. S.K.P. acknowledges the SERB, J C Bose Fellowship and DST for the financial support.

REFERENCES

(1) Kingon, A. I.; Maria, J.-P.; Streiffer, S. K. Alternative dielectrics to silicon dioxide for memory and logic devices. *Nature* **2000**, *406*, 1032–1038.

(2) Wang, Y.; Jie, W.; Yang, C.; Wei, X.; Hao, J. Colossal permittivity materials as superior dielectrics for diverse applications. *Adv. Funct. Mater.* **2019**, *29*, 1808118.

(3) Yim, K.; Yong, Y.; Lee, J.; Lee, K.; Nahm, H.-H.; Yoo, J.; Lee, C.; Seong Hwang, C.; Han, S. Novel high-κ dielectrics for next-generation electronic devices screened by automated ab initio calculations. *NPG Asia Mater.* **2015**, *7*, e190.

(4) Hao, X. A review on the dielectric materials for high energy-storage application. *J. Adv. Dielectr.* **2013**, *03*, 1330001.

(5) Palumbo, F.; Wen, C.; Lombardo, S.; Pazos, S.; Aguirre, F.; Eizenberg, M.; Hui, F.; Lanza, M. A review on dielectric breakdown in thin dielectrics: silicon dioxide, high-k, and layered dielectrics. *Adv. Funct. Mater.* **2019**, DOI: 10.1002/adfm.201900657.

(6) Roscow, J. I.; Bowen, C. R.; Almond, D. P. Breakdown in the case for materials with giant permittivity? *ACS Energy Lett.* **2017**, *2*, 2264−2269.
(7) Kim, B.-G.; Cho, S. M.; Kim, T.-Y.; Jang, H. M. Giant dielectric permittivity observed in Pb-based perovskite ferroelectrics. *Phys. Rev. Lett.* **2001**, *86*, 3404−3406.
(8) Pecharromán, C.; Esteban-Betegón, F.; Bartolomé, J. F.; López-Esteban, S.; Moya, J. S. New Percolative $BaTiO_3$−Ni Composites with a high and frequency-independent dielectric constant ($\epsilon_r \approx 80000$). *Adv. Mater.* **2001**, *13*, 1541−1544.
(9) Yan, Y.; Zhou, J. E.; Maurya, D.; Wang, Y. U.; Priya, S. Giant piezoelectric voltage coefficient in grain-oriented modified $PbTiO_3$ material. *Nat. Commun.* **2016**, *7*, 13089.
(10) Yu, J.; Ishikawa, T.; Arai, Y.; Yoda, S.; Itoh, M.; Saita, Y. Extrinsic origin of giant permittivity in hexagonal $BaTiO_3$ single crystals: Contributions of interfacial layer and depletion layer. *Appl. Phys. Lett.* **2005**, *87*, 252904.
(11) Wang, Z.; Chen, X. M.; Ni, L.; Liu, X. Q. Dielectric abnormities of complex perovskite $Ba(Fe_{1/2}Nb_{1/2})O_3$ ceramics over broad temperature and frequency range. *Appl. Phys. Lett.* **2007**, *90*, 022904.
(12) Haeni, J. H.; Irvin, P.; Chang, W.; Uecker, R.; Reiche, P.; Li, Y. L.; Choudhury, S.; Tian, W.; Hawley, M. E.; Craigo, B.; et al. Room-temperature ferroelectricity in strained $SrTiO_3$. *Nature* **2004**, *430*, 758.
(13) Sarkar, S.; Jana, P. K.; Chaudhuri, B. K.; Sakata, H. Copper (II) oxide as a giant dielectric material. *Appl. Phys. Lett.* **2006**, *89*, 212905.
(14) Wu, J.; Nan, C.-W.; Lin, Y.; Deng, Y. Giant dielectric permittivity observed in Li and Ti doped NiO. *Phys. Rev. Lett.* **2002**, *89*, 217601.
(15) Krohns, S.; Lunkenheimer, P.; Kant, C.; Pronin, A. V.; Brom, H. B.; Nugroho, A. A.; Diantoro, M.; Loidl, A. Colossal dielectric constant up to gigahertz at room temperature. *Appl. Phys. Lett.* **2009**, *94*, 122903.
(16) Park, T.; Nussinov, Z.; Hazzard, K. R. A.; Sidorov, V. A.; Balatsky, A. V.; Sarrao, J. L.; Cheong, S.-W.; Hundley, M. F.; Lee, J. S.; Jia, Q. X.; et al. Novel dielectric anomaly in the hole-doped $La_2Cu_{1-x}Li_xO_4$ and $La_{2-x}Sr_xNiO_4$ insulators: signature of an electronic glassy state. *Phys. Rev. Lett.* **2005**, *94*, 017002.
(17) Hu, W.; Liu, Y.; Withers, R. L.; Frankcombe, T. J.; Norén, L.; Snashall, A.; Kitchin, M.; Smith, P.; Gong, B.; Chen, H.; et al. Electron-pinned defect-dipoles for high-performance colossal permittivity materials. *Nat. Mater.* **2013**, *12*, 821.
(18) Liu, J.; Duan, C. G.; Yin, W. G.; Mei, W. N.; Smith, R. W.; Hardy, J. R. Large dielectric constant and Maxwell-Wagner relaxation in $Bi_{2/3}Cu_3Ti_4O_{12}$. *Phys. Rev. B: Condens. Matter Mater. Phys.* **2004**, *70*, 144106.
(19) Adams, T. B.; Sinclair, D. C.; West, A. R. Giant barrier layer capacitance effects in $CaCu_3Ti_4O_{12}$ ceramics. *Adv. Mater.* **2002**, *14*, 1321−1323.
(20) Lunkenheimer, P.; Fichtl, R.; Ebbinghaus, S. G.; Loidl, A. Nonintrinsic origin of the colossal dielectric constants in $CaCu_3Ti_4O_{12}$. *Phys. Rev. B: Condens. Matter Mater. Phys.* **2004**, *70*, 172102.
(21) Subramanian, M. A.; Li, D.; Duan, N.; Reisner, B. A.; Sleight, A. W. High dielectric constant in $ACu_3Ti_4O_{12}$ and $ACu_3Ti_3FeO_{12}$ phases. *J. Solid State Chem.* **2000**, *151*, 323−325.
(22) Ramirez, A. P.; Subramanian, M. A.; Gardel, M.; Blumberg, G.; Li, D.; Vogt, T.; Shapiro, S. M. Giant dielectric constant response in a copper-titanate. *Solid State Commun.* **2000**, *115*, 217−220.
(23) Staresinic, D.; Lunkenheimer, P.; Hemberger, J.; Biljakovic, K.; Loidl, A. Giant dielectric response in the one-dimensional charge-ordered semiconductor $(NbSe_4)_3I$. *Phys. Rev. Lett.* **2006**, *96*, 046402.
(24) Blumberg, G.; Littlewood, P.; Gozar, A.; Dennis, B. S.; Motoyama, N.; Eisaki, H.; Uchida, S. Sliding density wave in $Sr_{14}Cu_{24}O_{41}$ ladder compounds. *Science* **2002**, *297*, 584−587.
(25) Federicci, R.; Hole, S.; Popa, A. F.; Brohan, L.; Baptiste, B.; Mercone, S.; Leridon, B. $Rb_2Ti_2O_5$: Superionic conductor with colossal dielectric constant. *Phys. Rev. Mater.* **2017**, *1*, 032001.
(26) Ahmad, M. M.; Yamada, K. Superionic PbSnF4: A giant dielectric constant material. *Appl. Phys. Lett.* **2007**, *91*, 052912.
(27) Ahmad, M. M.; Yamane, Y.; Yamada, K. Structure, ionic conduction, and giant dielectric properties of mechanochemically synthesized $BaSnF_4$. *J. Appl. Phys.* **2009**, *106*, 074106.
(28) Karamov, F. A. *Superionic conductors: heterostructures and elements of functional electronics based on them*; Cambridge International Science Publishing: Cambridge, U.K., 2008.
(29) Boyce, J. B.; Huberman, B. A. Superionic conductors: transitions, structures, dynamics. *Phys. Rep.* **1979**, *51*, 189−265.
(30) Owens, B. B.; Argue, G. R. High-conductivity solid electrolytes: MAg_4I_5. *Science* **1967**, *157*, 308−310.
(31) Boris, A.; Bredikhin, S. I. Interface charge transport and the electronic conductivity of $RbAg_4I_5$ solid electrolytes. *Solid State Ionics* **1990**, *40-41*, 269−271.
(32) Bredikhin, S.; Bondarev, V. N.; Boris, A. V.; Pikhitsa, P. V.; Weppner, W. Electronic conductivity and current instability in superionic crystals. *Solid State Ionics* **1995**, *81*, 19−28.
(33) Lidorenko, N. S.; Zil'bervarg, V. E.; Nagaev, E. L. Dielectric constants of solid electrolytes and transition to superionic state. *Sov. Phys. JETP* **1980**, *51*, 89−93.
(34) Geller, S. Crystal Structure of the Solid Electrolyte, $RbAg_4I_5$. *Science* **1967**, *157*, 310−312.
(35) Geller, S. Low-temperature phases of the solid electrolyte $RbAg_4I_5$. *Phys. Rev. B: Condens. Matter Mater. Phys.* **1976**, *14*, 4345−4355.
(36) Funke, K.; Banhatti, R. D.; Wilmer, D.; Dinnebier, R.; Fitch, A.; Jansen, M. Low-Temperature Phases of Rubidium Silver Iodide: Crystal structures and dynamics of the mobile silver ions. *J. Phys. Chem. A* **2006**, *110*, 3010−3016.
(37) Sarkar, A.; Chakrabarti, M.; Ray, S. K.; Bhowmick, D.; Sanyal, D. Positron annihilation lifetime and photoluminescence studies on single crystalline ZnO. *J. Phys.: Condens. Matter* **2011**, *23*, 155801.
(38) Kirkegaard, P., Pedersen, N. J.; Eldroup, M. *Report of Riso National Lab (Riso-M2740)*, 1989.
(39) Luitel, H.; Sanyal, D.; Gogurla, N.; Sarkar, A. Defect generation and recovery in polycrystalline ZnO during annealing below 300 °C as studied by in situ positron annihilation spectroscopy. *J. Mater. Sci.* **2017**, *52*, 7615−7623.
(40) Tahara, S.; Fukami, T. Anion polarization effects on static structure and ionic transport in superionic melt of $RbAg_4I_5$. *J. Phys. Soc. Jpn.* **2015**, *84*, 024602.
(41) Floros, S.; Liakopoulou-Kyriakides, M.; Karatasos, K.; Papadopoulos, G. E. Detailed study of the dielectric function of a lysozyme solution studied with molecular dynamics simulations. *Eur. Biophys. J.* **2015**, *44*, 599−611.
(42) Matsunaga, S. Structural features of superionic phase in AgBr-CuBr system by molecular dynamics simulation. *J. Phys.: Conf. Ser.* **2009**, *144*, 012011.
(43) Looser, H.; Mali, M.; Roos, J.; Brinkmann, D. Ag diffusion constant in $RbAg_4I_5$ and KAg_4I_5 determined by pulsed magnetic gradient NMR. *Solid State Ionics* **1983**, *9−10*, 1237−1240.
(44) Bentle, G. G. Silver diffusion in a high-conductivity solid electrolyte. *J. Appl. Phys.* **1968**, *39*, 4036−4038.
(45) Lederman, F. L.; Salamon, M. B.; Peisl, H. Evidence for an order-disorder transformation in the solid electrolyte $RbAg_4I_5$. *Solid State Commun.* **1976**, *19*, 147−150.
(46) Brinkmann, D.; Freudenreich, W.; Arend, H.; Roos, J. Evidence for a first-order phase transition at 209 K in the superionic conductor $RbAg_4I_5$. *Solid State Commun.* **1978**, *27*, 133−135.
(47) Gallagher, D. A.; Klein, M. V. Raman scattering studies in the solid electrolytes of the $RbAg_4I_5$ family. *Phys. Rev. B: Condens. Matter Mater. Phys.* **1979**, *19*, 4282.
(48) Vargas, R.; Coronel, G. W. First-order behavior of the 209 K phase transition of $RbAg_4I_5$. *Solid State Ionics* **1995**, *81*, 69−72.
(49) Dhar, J.; Sil, S.; Dey, A.; Ray, P. P.; Sanyal, D. Positron Annihilation Spectroscopic Investigation on the origin of temperature-dependent electrical response in methylammonium lead iodide perovskite. *J. Phys. Chem. Lett.* **2017**, *8*, 1745−1751.
(50) Sharon, M. *An introduction to the physics and electrochemistry of semiconductors: fundamentals and applications*; Wiley, 2016.
(51) Jonscher, A. K. The "universal" dielectric response. *Nature* **1977**, *267*, 673−679.

https://dx.doi.org/10.1021/acs.jpcc.0c02118
J. Phys. Chem. C 2020, 124, 9802−9809

(52) Jonscher, A. K. Dielectric relaxation in solids. *J. Phys. D: Appl. Phys.* **1999**, *32*, R57−R70.
(53) Mohanty, A.; Swain, D.; Govinda, S.; Row, T. N. G.; Sarma, D. D. Phase diagram and dielectric properties of $MA_{1-x}FA_xPbI_3$. *ACS Energy Lett.* **2019**, *4*, 2045−2051.

https://dx.doi.org/10.1021/acs.jpcc.0c02118
J. Phys. Chem. C 2020, 124, 9802−9809